nature materials

ARTICLES

https://doi.org/10.1038/s41563-022-01221-5

Check for updates

An efficient nickel hydrogen oxidation catalyst for hydroxide exchange membrane fuel cells

Weiyan Ni[1,6], Teng Wang[2,6], Florent Héroguel[3], Anna Krammer[4], Seunghwa Lee[1], Liang Yao[5], Andreas Schüler[4], Jeremy S. Luterbacher[3], Yushan Yan[2]✉ and Xile Hu[1]✉

The hydroxide exchange membrane fuel cell (HEMFC) is a promising energy conversion technology but is limited by the need for platinum group metal (PGM) electrocatalysts, especially for the hydrogen oxidation reaction (HOR). Here we report a Ni-based HOR catalyst that exhibits an electrochemical surface area-normalized exchange current density of 70 μA cm^{-2}, the highest among PGM-free catalysts. The catalyst comprises Ni nanoparticles embedded in a nitrogen-doped carbon support. According to X-ray and ultraviolet photoelectron spectroscopy as well as H_2 chemisorption data, the electronic interaction between the Ni nanoparticles and the support leads to balanced hydrogen and hydroxide binding energies, which are the likely origin of the catalyst's high activity. PGM-free HEMFCs employing this Ni-based HOR catalyst give a peak power density of 488 mW cm^{-2}, up to 6.4 times higher than previous best-performing analogous HEMFCs. This work demonstrates the feasibility of efficient PGM-free HEMFCs.

The proton exchange membrane fuel cell (PEMFC) is an emerging clean-energy technology, however, it requires heavy usage of Pt catalysts, perfluorinated membranes and acid-tolerant stack hardware, leading to high cost[1]. The hydroxide exchange membrane fuel cell (HEMFC) is potentially a cost-effective alternative to the PEMFC because less costly catalysts, membranes and stack hardware might be used in alkaline medium. One important target for the development of HEMFCs is to eliminate the need for platinum group metals (PGMs)[2]. To date, PGM-free catalysts for the oxygen reduction reaction (ORR) at the cathode have achieved performances comparable to their PGM counterparts[3–5], and highly conductive and stable hydroxide exchange membranes have emerged[6]. However, there is a lack of active PGM-free catalysts for the hydrogen oxidation reaction (HOR) at the anode, representing a major barrier to the progress of HEMFCs[2,7]. For example, HEMFCs with a PGM HOR catalyst and an Earth-abundant ORR catalyst can reach a peak power density of more than 2,500 mW cm^{-2} (ref. [5]), whereas HEMFCs with both PGM-free HOR and ORR catalysts have a highest peak power density of merely 76 mW cm^{-2} (ref. [8]). As a result, the US Department of Energy (DOE) has set a peak power density target of 600 mW cm^{-2} for PGM-free HEMFCs in 2030 (ref. [2]).

HEMFCs pose challenges for HOR catalysts, not only in having a high intrinsic activity, but also in exhibiting other desirable properties, such as a large surface area, porous structure and resistance to high temperature, anodic potential and CO poisoning[1]. Among Earth-abundant metals, nickel proves to be the best candidate to meet these requirements. Nevertheless, state-of-the-art Ni catalysts typically exhibit intrinsic activity below 40 μA per cm^2 electrochemical surface area (ECSA) of the catalyst (40 μA cm$_{cat}^{-2}$; refs. [9–11]). Although a few catalysts have a higher intrinsic activity, their surface areas are very small[12,13]. Furthermore, some catalysts exhibit good mass activity in model studies involving rotating disc electrode (RDE) measurements, but they are prone to oxidation and are unsuitable for practical devices[14]. In fact, the stability of nickel in a fuel cell working environment, that is, at elevated temperature and high current density, is not well demonstrated. As a result, previously reported Ni catalysts do not exhibit good performance in a complete cell configuration, especially with a PGM-free cathode. Here, we report a Ni catalyst that exhibits an intrinsic activity of 70 μA per cm^2 Ni (70 μA cm$_{Ni}^{-2}$). PGM-free HEMFCs employing this catalyst gave a peak power density of 488 mW cm^{-2} at 95 °C and 443 mW cm^{-2} at 80 °C, about six times higher than the previous best analogous HEMFCs. The superior activity of our catalyst is due to balanced hydrogen binding energy (HBE) and hydroxide binding energy (OHBE), resulting from a fine-tuned Ni–support interaction.

The catalyst Ni-H_2-NH_3 was prepared by pyrolysing a Ni-based metal–organic framework, $Ni_3(BTC)_2$ (BTC, benzene-1,3,5-tricarboxylate)[14], at 390 °C in a mixed atmosphere of H_2/NH_3/N_2 (4.6:33.6:61.8, v/v/v; see Materials and methods and Supplementary Figs. 1–3). NH_3 was used to introduce nitrogen doping to regulate the electronic structure of Ni (ref. [9]), while H_2 was used as a reducing agent to form metallic Ni. The temperature and partial pressure of each gas were carefully optimized. Reference compounds Ni-H_2 and Ni-NH_3 were also prepared using the same method with H_2/N_2 and NH_3/N_2 ratios of 4.6:95.4 and 33.6:66.4 (v/v), respectively (Fig. 1a).

Transmission electron microscopy (TEM) showed that Ni-H_2-NH_3 and Ni-NH_3 contained small, separated nanoparticles with an average size of 13.3 ± 3.5 and 8.6 ± 2.1 nm, respectively, whereas Ni-H_2 was composed of sintered particles with a large grain size (Fig. 1b–d and Supplementary Fig. 4). The Supplementary Notes and Supplementary Figs. 5–10 provide additional characterization data for Ni-H_2-NH_3, Ni-NH_3 and Ni-H_2. High-resolution

[1]Laboratory of Inorganic Synthesis and Catalysis, Institute of Chemical Sciences and Engineering, École Polytechnique Fédérale de Lausanne (EPFL), Lausanne, Switzerland. [2]Department of Chemical and Biomolecular Engineering, University of Delaware, Newark, DE, USA. [3]Laboratory of Sustainable and Catalytic Processing, Institute of Chemical Sciences and Engineering, École Polytechnique Fédérale de Lausanne (EPFL), Lausanne, Switzerland. [4]Solar Energy and Building Physics Laboratory, Institute of Civil Engineering, École Polytechnique Fédérale de Lausanne (EPFL), Lausanne, Switzerland. [5]Laboratory for Molecular Engineering of Optoelectronic Nanomaterials, Institute of Chemical Sciences and Engineering, Ecole Polytechnique Fédérale de Lausanne (EPFL), Lausanne, Switzerland. [6]These authors contributed equally: Weiyan Ni, Teng Wang. ✉e-mail: yanys@udel.edu; xile.hu@epfl.ch

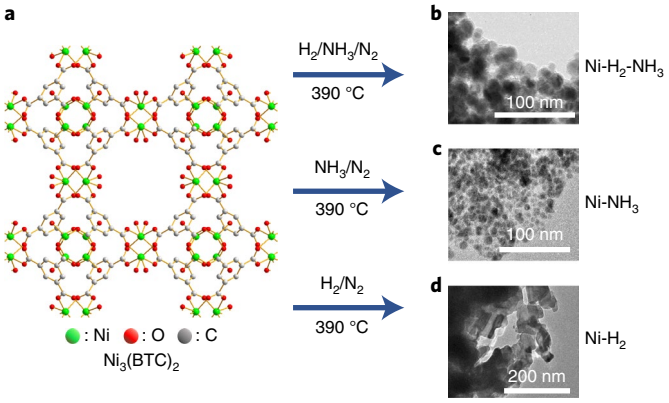

Fig. 1 | Synthesis and TEM images of the Ni catalysts. a, Schematic illustration of the synthesis of the Ni catalysts. **b**–**d**, TEM images of Ni-H_2-NH_3 (**b**), Ni-NH_3 (**c**) and Ni-H_2 (**d**).

Ni $2p_{3/2}$ X-ray photoelectron spectroscopy (XPS) revealed that all three compounds exhibited shifted metallic Ni(0) peaks compared with that of bulk, unsupported Ni as reference, indicative of interfacial charge transfer from Ni to the carbon support[15] (see XPS spectra in the Supplementary Notes and Supplementary Fig. 11). By comparing the intensity ratios of different Raman bands, we concluded that Ni-NH_3 had a more disordered carbon support than Ni-H_2-NH_3 and Ni-H_2 (see Raman spectra in the Supplementary Notes, Supplementary Fig. 12 and Supplementary Table 2). This conclusion was supported by high-resolution TEM (HRTEM) images, which showed lattice fringes for the carbon support of Ni-H_2-NH_3 and Ni-H_2, but not for Ni-NH_3 (Supplementary Fig. 13). Disordered carbon might lead to a lower conductivity. Indeed, four-probe electrical conductivity measurements revealed that Ni-NH_3 had a sheet resistance one order of magnitude higher than Ni-H_2-NH_3 and Ni-H_2 (Supplementary Fig. 14).

The electrochemical HOR activity of the three nickel catalysts was evaluated in H_2-saturated 0.1 M KOH and compared with that of commercial 20 wt% Pt/C (Fig. 2a). The activity of the three Ni catalysts decreased in the following order: Ni-H_2-NH_3 > Ni-NH_3 > Ni-H_2. The linear sweep voltammetry (LSV) curve of Ni-H_2-NH_3 approached that of 20 wt% Pt/C, a benchmark PGM catalyst. Comparison of the LSV curves in N_2- and H_2-saturated 0.1 M KOH confirmed that the anodic current density observed for Ni-H_2-NH_3 in Fig. 2a originated from hydrogen oxidation (Supplementary Fig. 15).

The kinetic parameters of the HOR were extracted using Koutecky–Levich and Butler–Volmer equations (Fig. 2b and Materials and methods). This analysis yielded two parameters that can be used to compare different catalysts: the apparent mass activity at a given overpotential (Supplementary Fig. 16) and the electrochemical surface area (ECSA)-normalized exchange current density ($j_{0,ECSA}$; also see ECSA analysis in the Supplementary Notes and Supplementary Fig. 17). Ni-H_2-NH_3 showed a mass-averaged current density of 59.2 mA per mg Ni (59.2 mA mg_{Ni}^{-1}) at an overpotential (η) of 50 mV, and a $j_{0,ECSA}$ value of 70 μA cm_{Ni}^{-2}. The intrinsic activity, $j_{0,ECSA}$, is the highest among Ni-based HOR catalysts, and is even higher than a modified Pd catalyst (Table 1 and Supplementary Table 3). Ni-H_2-NH_3 is also an excellent HER catalyst, with high activity and good stability (Supplementary Fig. 18 and Supplementary Table 3).

An accelerated durability test was conducted by performing 1,000 cyclic voltammetric (CV) scans from −0.15 to 0.1 V versus the reversible hydrogen electrode (RHE) at a scan rate of 100 mV s^{-1}. LSV curves showed that Ni-H_2-NH_3 experienced only a small decrease in HOR activity after this process (Fig. 2c). Detailed kinetic analysis indicated that $j_{0,disc}$ decreased to 82% of its original value. In contrast, LSV curves indicated a significant decrease in HOR activity for Ni-NH_3 after 1,000 CV scans, and $j_{0,disc}$ decreased to 38% of its original value. CO resistivity was also tested on Ni-H_2-NH_3 and Pt/C (20 wt%) by LSV in an electrolyte purged with H_2 gas containing 7.5 vol% N_2 or CO. Both materials suffered from CO poisoning, but Ni-H_2-NH_3 was clearly less affected, suggesting a better CO resistivity (Fig. 2d). In addition, the HOR on Ni-H_2-NH_3 was resistant to high anodic potentials, as it could maintain a current density of 3 mA cm^{-2} up to 0.23 V versus RHE (Supplementary Fig. 19).

Because adsorbed hydrogen (H_{ads}) is a key intermediate in the HOR, the HBE has been proposed as a descriptor of catalytic activity[16]. However, simple HBE theory cannot explain several of the experimental findings, such as the pH-dependent activity of PGMs[17,18] and the enhanced activity of transition metal hydr(oxy) oxide-decorated PGMs[19–21]. Yan and co-workers proposed the apparent HBE (HBE_{app}) theory, whereby the HBEs are corrected by a term related to the change in Gibbs free energy of interfacial water[17,22–24]. The importance of water reorganization for the HOR on PGMs has been recognized in several other studies[25–27], with some of them proposing the interfacial electric field as the origin of the different water reorganization energies in acid and basic media[25,26]. In parallel, the OHBE theory, where adsorbed hydroxyl species (OH_{ads}) facilitate the removal of H_{ads} in alkaline medium, was proposed for PGM–metal oxide composites[21]. There is some debate as to whether OH_{ads} is universally involved in the HOR in alkaline medium[27–30], and recently effort has been made to unify the HBE and OHBE theories[31,32]. McCrum and Koper proposed that when the OHBE is very low, OH_{ads} is not involved in the HOR, but the activation barrier of the Volmer step (proportional to HBE_{app}) correlates with the OHBE. When the OHBE is high, then both H_{ads} and OH_{ads} are involved. Thus, the OHBE can be used as an overall descriptor[31]. The above theories, still in the stage of development[18], have been developed mostly for PGMs (especially Pt), which could be different from Ni. In the present study, we attempted to probe experimentally whether some of these theories could explain the activity of our catalysts.

We probed the electronic states of Ni-H_2, Ni-NH_3, Ni-H_2-NH_3 and an unsupported Ni reference. The XPS data have already indicated an interfacial charge transfer from Ni to the carbon support for Ni-H_2-NH_3, Ni-NH_3 and Ni-H_2. The transfer originates from the difference in the work functions of Ni and carbon, and results in the hybridization of the 3*d* states of Ni with the π-states of carbon[33]. This interaction alters the electronic structure of Ni and shifts its *d* band further away from the Fermi level compared with pure Ni (ref. [34]). XPS probes the binding energies of core electrons, whereas the adsorption energies of reaction intermediates are more influenced by valence electrons. Thus, we further examined the valence-state structure of Ni using ultraviolet photoelectron spectroscopy (UPS). All four Ni samples have electron bands crossing the Fermi level (Fig. 3a), indicative of their metallic nature[35,36]. The peaks next to the Fermi level correspond to metallic Ni 3*d* states. Their positions, corresponding to their binding energy, shift away from the Fermi level in the following order: Ni < Ni-H_2 < Ni-H_2-NH_3 < Ni-NH_3 (Supplementary Fig. 20). According to *d*-band theory, a down-shifted *d*-band leads to weakened adsorption strength[37]. Thus, the HBE and OHBE should follow the order Ni > Ni-H_2 > Ni-H_2-NH_3 > Ni-NH_3.

We probed the HBE through H_2 chemisorption (see H_2 chemisorption in the Supplementary Notes, Supplementary Fig. 21 and Supplementary Table 4), with Pt/C as an additional reference. The adsorption behaviour could be described by a dual Langmuir model, which assumes that the adsorption consists of strong adsorption (that is, chemisorption) and weak adsorption (that is,

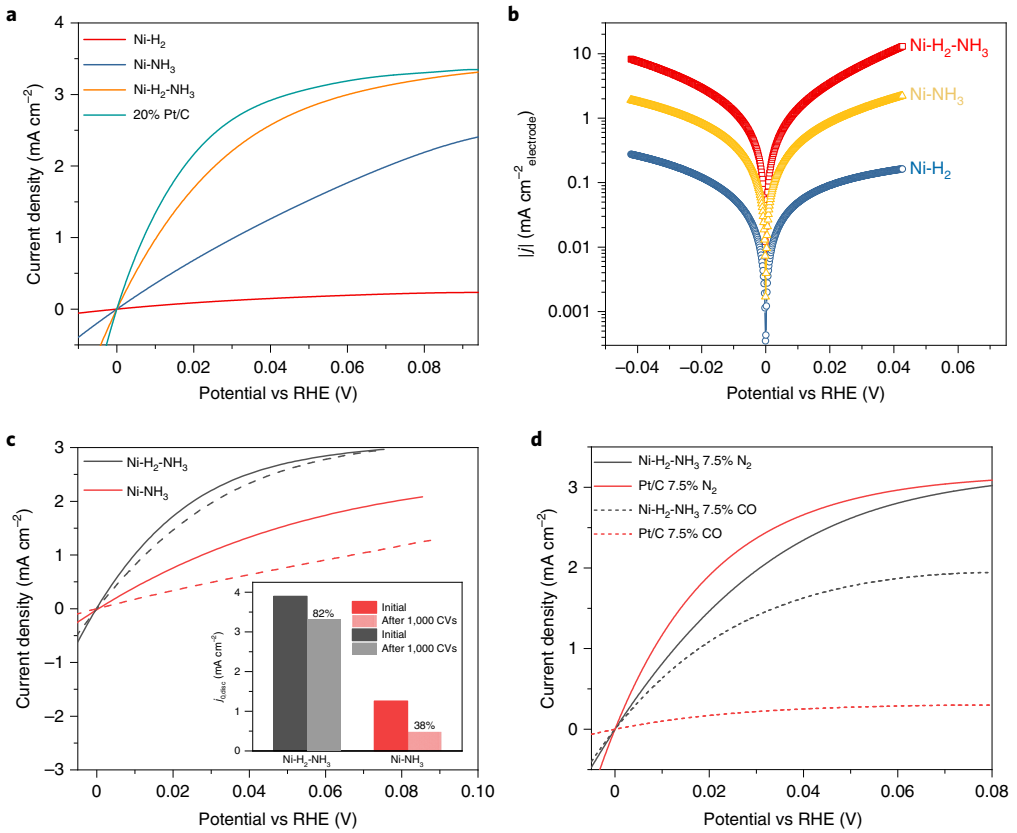

Fig. 2 | Electrochemical HOR. a, HOR polarization curves for Ni-H_2-NH_3, Ni-NH_3, Ni-H_2 and commercial Pt/C (20 wt%) for an electrode rotating speed of 2,500 r.p.m. **b**, Butler–Volmer plots of the HOR current densities shown in **a**. **c**, Accelerated durability test for the HOR in the presence of Ni-H_2-NH_3 and Ni-NH_3. The solid curve is the initial LSV, and the dashed curve is the LSV after the durability test. Inset: the bar plot shows a comparison of $j_{0,disc}$ before and after 1,000 CV scans. **d**, CO poisoning experiments for Ni-H_2-NH_3 and 20 wt% Pt/C. Five LSV scans were performed in the CO-containing electrolyte before recording the HOR polarization curve.

Table 1 | Comparison of state-of-the-art Pt-free HOR catalysts

Catalyst	Mass activity at $\eta = 50$ mV (mA mg_{cat}^{-1})	$j_{0,ECSA}$ (μA cm_{cat}^{-2})	Reference
Ni-H_2-NH_3	**59.2**	**70**	**This work**
Ni-NH_3	**12.7**	**20**	
Ni-H_2	**0.8**	**18**	
Ni_3N/C	24.4	14	15
np-Ni_3N	29.8	-	42
Ni-H_2-2%	50.4	28	14
CeO_2(r)-Ni/C-1	12.3	38	11
Ni/NiO/C-700	5.0	26	10
Ni/N-CNT	9.3	28	9
Ni/Ni_3N/NF	-	3	43
Pd/C-CeO_2	-	54.5	44

physisorption). Our fitting results showed that the hydrogen binding strength follows the order Ni ≫ Ni-H_2 > Ni-H_2-NH_3 > Ni-NH_3 > Pt/C (Fig. 3b). These data agree with the prediction of *d*-band theory.

We then probed whether OHBE was relevant for the HOR on our catalysts through isotope experiments. We tested the HOR on Ni-H_2-NH_3 in deuterated electrolytes (Fig. 3c and Isotopic study in the Supplementary Notes). After removing the diffusion overpotential with the Koutecky–Levich equation, the Butler–Volmer plots of ECSA-normalized current densities revealed a more than twofold lower kinetic current density in 0.1 M KOD compared with in 0.1 M KOH (Fig. 3d). The slower kinetics of the HOR on Ni-H_2-NH_3 in deuterated electrolytes might be due to the following four factors: (1) a primary kinetic isotope effect (KIE), (2) a stronger interfacial electric field and hence slower water reorganization in KOD due to a more negative equilibrium potential than in KOH[25,26], (3) a weaker OH binding in KOD and (4) different solvent dynamics of D_2O compared with H_2O (refs. [18,27]). As the kinetic current density ratio $j_k(H_2O)/j_k(D_2O)$ increased with potential, we ruled out the KIE (Supplementary Fig. 22 and Isotopic study in the Supplementary Notes). The reversible deuterium electrode (RDeuE) potential of 0.1 M KOD is similar to the RHE of 1 M KOH, and the kinetics of the HOR are similar in 0.1 and 1 M KOH solutions (Fig. 3c). These data exclude a stronger interfacial electric field as the origin of the H/D isotope effect (see Isotopic study in the Supplementary Notes). We measured the OHBE in KOD and KOH by electrochemical OH chemisorption. Anodic peaks located in the range 0.2–0.4 V versus RHE are generally assigned to the oxidative adsorption of OH species, and a higher potential indicates a weaker OH binding[15,38]. As shown in Fig. 3e, the OHBE is similar in 0.1 and 1 M KOH, consistent with the similar HOR activity in these two electrolytes. However, the deuteroxide binding energy (ODBE) is much more positive in 0.1 M KOD, with an oxidative adsorption peak shift of about 75 mV (Fig. 3e). The positive shift of peak potential agrees with the better oxidative resistance of Ni-H_2-NH_3 in 0.1 M KOD compared with in 0.1 M KOH (Fig. 3c). The more positive

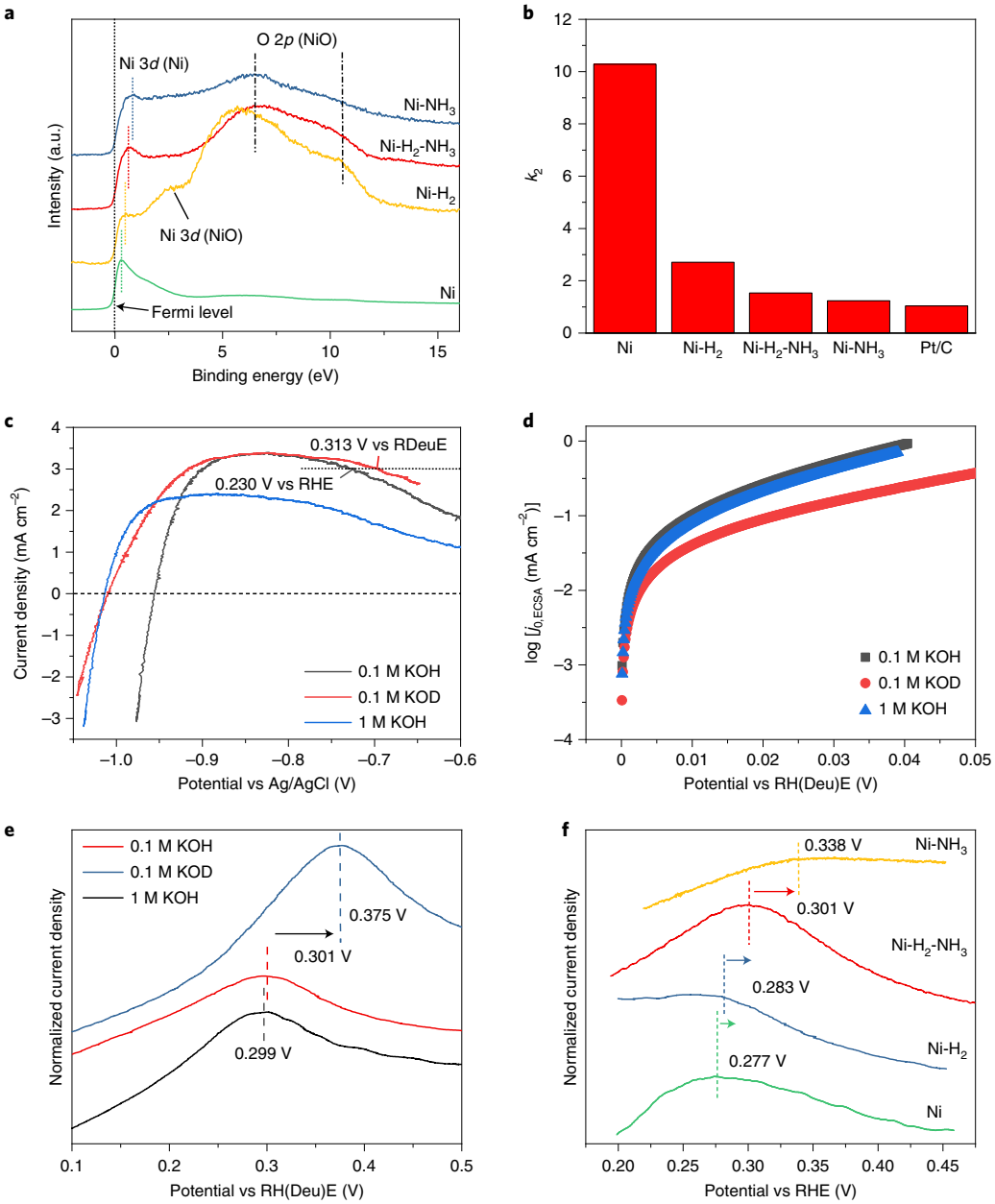

Fig. 3 | Mechanistic studies. a, UPS spectra of Ni-H_2-NH_3, Ni-NH_3, Ni-H_2 and a Ni reference. **b**, Representation of the strong adsorption equilibrium constant k_2 determined by H_2 chemisorption for Ni-H_2-NH_3, Ni-NH_3, Ni-H_2 and Ni and Pt/C references. **c**, Polarization curves for Ni-H_2-NH_3 in H_2-saturated 0.1 M KOH, 0.1 M KOD and 1 M KOH solutions. The horizontal dashed line indicates the potential where the current reaches 3 mA cm^{-2}. **d**, Butler–Volmer plots of ECSA-normalized current densities derived from **c**. RH(Deu)E, RHE or RDeuH. **e**, Anodic scans of Ni-H_2-NH_3 showing $OH(D)^-$ oxidative adsorption in N_2-saturated KOH or KOD solution. **f**, Anodic scans showing the oxidative adsorption of OH^- in N_2-saturated KOH solution for Ni-H_2-NH_3, Ni-NH_3, Ni-H_2 and Ni.

ODBE is probably due to a stronger O–D bond[39], which makes OD^- a weaker nucleophile than OH^-. These data are consistent with the OHBE being the origin of the H/D isotope effect on Ni-H_2-NH_3. Tang and co-workers observed similar H/D isotope effects on Pt. Although they attributed these effects to solvent dynamics, they also observed a lower OHBE in KOD compared with in KOH[27]. As we were not able to measure the binding strength of water on our nickel samples using surface-enhanced Infrared adsorption spectroscopy (SEIRAS), we could not rule out solvent dynamics as an additional contributor to the H/D isotope effects. Despite this uncertainty, the H/D isotope effects indicate the OHBE to be a relevant parameter for understanding the activity of Ni-H_2-NH_3, and by analogy, the other Ni-based catalysts in this work. We also recognize at the molecular level under dynamic conditions that OH and water adsorption may follow the same trend.

We then determined the OHBE by OH chemisorption (Fig. 3f). The OHBE decreases in the following order: Ni > Ni-H_2 > Ni-H_2-NH_3 > Ni-NH_3. This order is consistent with the prediction of *d*-band theory. The presence of OH_{ads} was supported by the in situ observation of a peak located at ~727 cm^{-1} in shell-isolated nanoparticles-enhanced Raman (SHINER) spectra of Ni-H_2-NH_3 at potentials relevant to the HOR and HER (Supplementary Fig. 23)[40]. Deuterium isotopic substitution experiments confirmed the peak assignment (Supplementary Fig. 23).

Using the chemisorption binding constant as a proxy for HBE, we correlated the HOR activity ($j_{0,ECSA}$) with HBE (Fig. 4a).

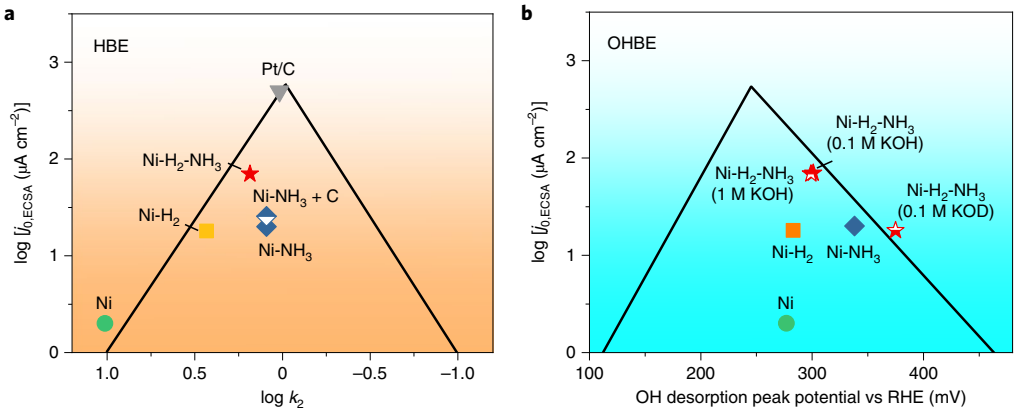

Fig. 4 | Correlation of measured HOR activities with HBEs and OHBEs. a, Plot of the logarithm of k_2 obtained in Fig. 3b as a proxy for HBE versus the logarithm of the measured exchange current densities of nickel samples and platinum. **b**, Plot of the OH desorption peak potential of nickel samples measured in Fig. 3e,f as a proxy for OHBE versus the logarithm of measured exchange current densities. The solid lines in both **a** and **b** are indicative and are meant to mimic previously reported HBE and OHBE volcano plots[31].

The benchmark Pt/C catalyst was assumed to have an optimal HBE, sitting at the top of the volcano plot predicted by HBE theory. The activity trend of the Ni-based catalysts deviated from the volcano plot. In particular, Ni-NH_3 was predicted to have the best activity, but in reality, it is much worse than that of Ni-H_2-NH_3. We ruled out a high surface oxide coverage as the origin of the low activity of Ni-NH_3. Rather, its poor conductivity was found to undermine the HOR performance (see Ni-NH_3 in the Supplementary Notes). Nevertheless, its activity was still much lower than Ni-H_2-NH_3 even after the addition of conductive carbon black (Supplementary Fig. 24). The poor correlation of HOR activity with HBE suggests that the activity of the Ni catalysts described here cannot be explained by a single HBE descriptor. We attempted, but were unable to probe the binding strength of water on our nickel samples using SEIRAS (ref. [3]), so we could not experimentally test whether the HBE_{app} theory could explain the activity of our catalysts.

We tried to correlate the HOR activity with OHBE, taking the potential of OH^- adsorption as a proxy for OHBE (Fig. 4b). Consistent with the literature[10,11,41], we assumed that the OHBEs of the Ni-based catalysts are on the low side. Once again, the HOR activity deviated from the predicted volcano plot based on a single OHBE descriptor. In particular, the experimental order of activity of Ni < Ni-H_2 < Ni-H_2-NH_3 is opposite to the prediction by OHBE theory.

Our results are, however, consistent with a combination of HBE and OHBE theory, where both H_{ads} and OH_{ads} play an important role in the Volmer step[28,32]. From Ni to Ni-H_2 to Ni-H_2-NH_3, the HBE decreased substantially, whereas the OHBE decreased to a lesser extent. The effect of HBE dominates so that the activity follows the trend of Ni < Ni-H_2 < Ni-H_2-NH_3. From Ni-H_2-NH_3 to Ni-NH_3, the HBE decreased to a lesser extent than OHBE, so the effect of OHBE dominates, leading to a much lower activity of Ni-NH_3. Therefore, the optimal HOR activity of Ni-H_2-NH_3 is a result of an optimized balance between low HBE and low OHBE. Because *d*-band tuning changes the HBE and OHBE in a synchronized manner, these results suggest that further improvement of Ni-based catalysts might be achieved by designing catalysts where HBE and OHBE can be varied independently.

The Ni catalysts were synthesized by pyrolysis of the same precursor in different gas atmospheres. We probed how the gases influenced the properties and activity of the catalysts. The main function of NH_3 seemed to be the production of N-doped carbon, which according to our UPS data, downshifts the *d* band of Ni, leading to lower binding energies of adsorbates. A similar effect was observed previously[9,42,43], and was suggested to originate from the Ni–support interaction and scale with the interfacial contact surface area[9,44]. The Ni nanoparticles in Ni-H_2-NH_3 are partially embedded in the carbon support (Supplementary Fig. 6a), which results in a high interfacial area. The larger interfacial contact area leads to more effective tuning of Ni's electronic properties. The extent of the *d*-band shift correlates with the N content (Supplementary Table 1). Adding H_2 prevents the overdoping of nitrogen, leading to a modest N content, and hence an optimal shift of the *d* band. NH_3 has two additional counterbalancing roles: (1) it prevents the sintering of particles so that Ni-H_2-NH_3 and Ni-NH_3 are made of much smaller and more evenly distributed particles than Ni-H_2 (Fig. 1b–d) and (2) it leads to a poorly graphitized carbon support, as seen in the elemental analysis results (Supplementary Table 1), Raman spectra (Supplementary Table 2) and HRTEM images (Supplementary Fig. 13). The poor graphitization leads to low conductivity (Supplementary Fig. 14) and stability (Fig. 2c and Supplementary Fig. 18). The low conductivity of Ni-NH_3 is detrimental to its catalytic activity (Supplementary Fig. 24). Adding H_2 to NH_3 resulted in both good graphitization and small particle size, combining the benefits of both NH_3 and H_2, while avoiding their pitfalls.

We incorporated Ni-H_2-NH_3 into a membrane electrode assembly (MEA) comprising a state-of-the-art poly(arylpiperidinium)-based polymer as membrane and ionomer for HEMFC performance testing[6]. We employed CoMn spinel as the ORR catalyst in the PGM-free MEA (Supplementary Figs. 25 and 26)[3,45]. The as-prepared $MnCo_2O_4$/C catalyst showed good ORR activity, with a half-wave potential only 13 mV lower than a commercial Pt/C catalyst in a RDE configuration (Supplementary Fig. 27). With Ni-H_2-NH_3 as anode, $MnCo_2O_4$/C as cathode and O_2 as cathodic gas feed, the PGM-free HEMFC delivered a current density of 606 mA cm^{-2} at 0.65 V (estimated operating cell voltage was constrained by heat rejection in the stack) and reached a high peak power density (PPD) of 488 mW cm^{-2} (Fig. 5a), 6.4 times higher than the previous record for analogous HEMFCs (Fig. 5b and Supplementary Table 5)[8]. Replacing O_2 by air as cathodic gas feed gave a high PPD of 310 mW cm^{-2} and approaches the 600 mW cm^{-2} target set by the US DOE for 2030 (ref. [2]). For a better comparison with literature data[8], we tested the MEA at 80 °C with H_2/O_2 gas feed (Supplementary Fig. 28). The resulting PPD was 443 mW cm^{-2}, still 5.8 times higher than the previous record. The promising performance of our PGM-free HEMFC indicates the feasibility of efficient HEMFCs without PGM catalysts[46–48].

We also assembled MEAs with PGM ORR catalysts and measured their performance. When using 0.2 mg cm^{-2} Pt/C as cathode and O_2

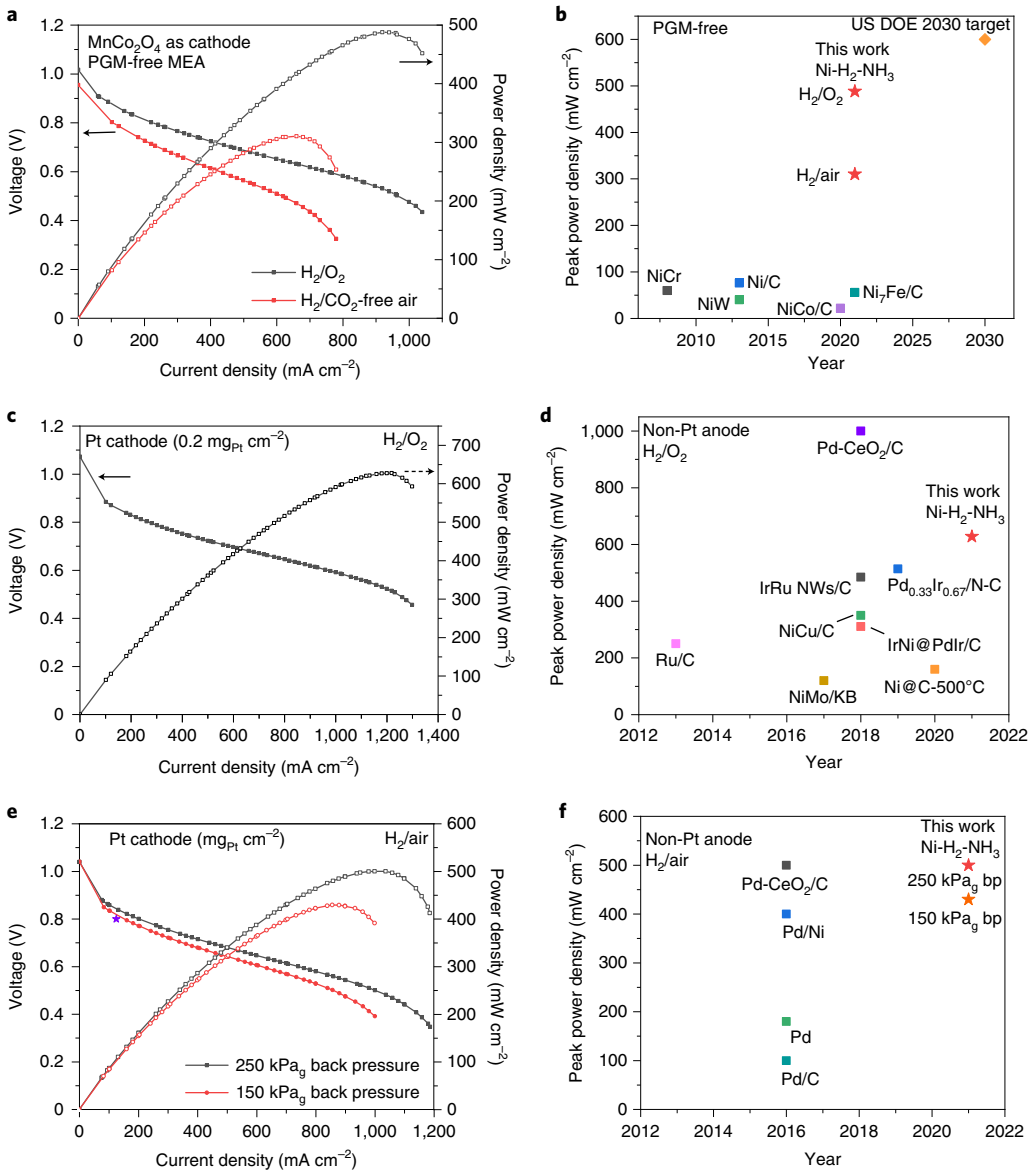

Fig. 5 | Hydrogen fuel cell performance using Ni-H_2-NH_3 as anode. a, PGM-free H_2/O_2 HEMFC performance using CoMn spinel as the cathode catalyst. Test conditions: cell temperature 95.0 °C, cathode humidifier 96.0 °C, anode humidifier 88.0 °C, H_2 flow rate 0.2 l min^{-1} and O_2/air flow rate 0.2/1 l min^{-1} with 250 kPa_g back pressure on both sides. **b**, Comparison of our PGM-free MEA test results with previously reported data (all tested with H_2/O_2 gas feed). Details are listed in Supplementary Table 5. **c**, Polarization and power density curves using Pt/C as the cathode material. Test conditions were the same as in **a**. **d**, Comparison of our MEA test results with other non-Pt anode MEA performances with H_2/O_2 gas feed. These MEAs used a Pt, Pd or Ag cathode. Details are listed in Supplementary Table 6. **e**, H_2/CO_2-free air fuel cell performance using Ni-H_2-NH_3 as anode and Pt/C (0.2 mg Pt per cm^2) as cathode. Test conditions: cell temperature 95 °C, cathode humidifier 96.0 °C, anode humidifier 88.0 °C, H_2 flow rate 0.2 l min^{-1} and air flow rate 1 l min^{-1} with specific back pressure on both sides. The purple star marks the US DOE 2021 target for HEMFCs[2]. **f**, Comparison of our MEA test results with other non-Pt anode MEA performances with H_2/air gas feed. bp, back pressure.

as cathodic gas feed, the fuel cell delivered a PPD of 628 mW cm^{-2} (Fig. 5c) and a current density of 780 mA cm^{-2} at 0.65 V. This performance exceeds all the previously reported fuel cells with a Ni anode, and it is even comparable to some recently reported fuel cells with a non-Pt PGM anode (Fig. 5d and Supplementary Table 6). The performance of this MEA at 80 °C was also excellent, with a PPD of 560 mW cm^{-2} (Supplementary Fig. 28, 29, 30, 31). H_2/air feeds were employed to match the test conditions of the US DOE 2021 target for HEMFCs, which demanded a power density of 100 mW cm^{-2} (equivalent to a current density of 125 mA cm^{-2}) at 0.8 V with H_2/air gas feeds (≤150 kPa gauge (kPa_g) pressure) for the HEMFC with PGM loading no more than 0.2 mg cm^{-2} (ref. [2]). Our MEA with a power density of 120 mW cm^{-2} (Fig. 5e) measured at 150 kPa_g (kPa_g under this specific condition) surpassed the targeted value. Increasing the back pressure to 250 kPa_g resulted in a power density of 160 mW cm^{-2} at 0.8 V, a current density of 590 mA cm^{-2} at 0.65 V and a PPD of 500 mW cm^{-2}. This performance is comparable to MEAs using advanced Pd catalysts (Fig. 5f and Supplementary Table 6). By comparing with the literature (Supplementary Table 7), we found that our MEA has one of the highest PGM utilization values observed to date (Supplementary Fig. 29 and PGM utilization in the Supplementary Notes). Moreover, durability testing of this HEMFC at 95 °C with a constant voltage of 0.7 V showed only 7% degradation of current density after 40 h (Supplementary Fig. 30),

demonstrating the ability of our catalyst to work steadily under high temperature and large current. Pt migration to the Ni-based anode in the fuel cell test was excluded by XPS analysis of the anode surface after the durability test (Supplementary Fig. 31). Meanwhile, the metallic nanoparticles in Ni-H_2-NH_3 were stable after the durability test (Supplementary Fig. 32). Overall, the superior activity and robustness of our new Ni catalyst under device-relevant conditions demonstrate the potential of Earth-abundant HOR catalysts for the development of efficient PGM-free HEMFCs.

Online content

Any methods, additional references, Nature Research reporting summaries, source data, extended data, supplementary information, acknowledgements, peer review information; details of author contributions and competing interests; and statements of data and code availability are available at https://doi.org/10.1038/s41563-022-01221-5.

Received: 8 January 2021; Accepted: 16 February 2022;
Published online: 04 April 2022

References

1. Setzler, B. P., Zhuang, Z., Wittkopf, J. A. & Yan, Y. Activity targets for nanostructured platinum-group-metal-free catalysts in hydroxide exchange membrane fuel cells. *Nat. Nanotechnol.* **11**, 1020–1025 (2016).
2. Thompson, S. T., Peterson, D., Ho, D. & Papageorgopoulos, D. Perspective—the next decade of AEMFCs: near-term targets to accelerate applied R&D. *J. Electrochem. Soc.* **167**, 084514 (2020).
3. Wang, Y. et al. Synergistic Mn–Co catalyst outperforms Pt on high-rate oxygen reduction for alkaline polymer electrolyte fuel cells. *Nat. Commun.* **10**, 1506 (2019).
4. Santori, P. G. et al. High performance FeNC and Mn-oxide/FeNC layers for AEMFC cathodes. *J. Electrochem. Soc.* **167**, 134505 (2020).
5. Peng, X. et al. High-performing PGM-free AEMFC cathodes from carbon-supported cobalt ferrite nanoparticles. *Catalysts* **9**, 264 (2019).
6. Wang, J. et al. Poly(aryl piperidinium) membranes and ionomers for hydroxide exchange membrane fuel cells. *Nat. Energy* **4**, 392–398 (2019).
7. Firouzjaie, H. A. & Mustain, W. E. Catalytic advantages, challenges, and priorities in alkaline membrane fuel cells. *ACS Catal.* **10**, 225–234 (2019).
8. Gu, S. et al. An efficient Ag–ionomer interface for hydroxide exchange membrane fuel cells. *Chem. Commun.* **49**, 131–133 (2013).
9. Zhuang, Z. et al. Nickel supported on nitrogen-doped carbon nanotubes as hydrogen oxidation reaction catalyst in alkaline electrolyte. *Nat. Commun.* **7**, 10141 (2016).
10. Yang, Y. et al. Enhanced electrocatalytic hydrogen oxidation on Ni/NiO/C derived from a nickel-based metal–organic framework. *Angew. Chem. Int. Ed.* **58**, 10644–10649 (2019).
11. Yang, F. et al. Boosting hydrogen oxidation activity of Ni in alkaline media through oxygen-vacancy-rich CeO_2/Ni heterostructures. *Angew. Chem. Int. Ed.* **58**, 14179–14183 (2019).
12. Davydova, E., Zaffran, J., Dhaka, K., Toroker, M. & Dekel, D. Hydrogen oxidation on Ni-based electrocatalysts: the effect of metal doping. *Catalysts* **8**, 454 (2018).
13. Oshchepkov, A. G. et al. Nanostructured nickel nanoparticles supported on vulcan carbon as a highly active catalyst for the hydrogen oxidation reaction in alkaline media. *J. Power Sources* **402**, 447–452 (2018).
14. Ni, W. et al. Efficient hydrogen oxidation catalyzed by strain-engineered nickel nanoparticles. *Angew. Chem. Int. Ed.* **59**, 10797–10801 (2020).
15. Ni, W. et al. Ni_3N as an active hydrogen oxidation reaction catalyst in alkaline medium. *Angew. Chem. Int. Ed.* **58**, 7445–7449 (2019).
16. Durst, J. et al. New insights into the electrochemical hydrogen oxidation and evolution reaction mechanism. *Energy Environ. Sci.* **7**, 2255–2260 (2014).
17. Zheng, J., Sheng, W., Zhuang, Z., Xu, B. & Yan, Y. Universal dependence of hydrogen oxidation and evolution reaction activity of platinum-group metals on pH and hydrogen binding energy. *Sci. Adv.* **2**, e1501602 (2016).
18. Rebollar, L. et al. "Beyond adsorption" descriptors in hydrogen electrocatalysis. *ACS Catal.* **10**, 14747–14762 (2020).
19. Subbaraman, R. et al. Enhancing hydrogen evolution activity in water splitting by tailoring Li^+–$Ni(OH)_2$–Pt interfaces. *Science* **334**, 1256–1260 (2011).
20. Subbaraman, R. et al. Trends in activity for the water electrolyser reactions on 3*d* M(Ni,Co,Fe,Mn) hydr(oxy)oxide catalysts. *Nat. Mater.* **11**, 550–557 (2012).
21. Strmcnik, D. et al. Improving the hydrogen oxidation reaction rate by promotion of hydroxyl adsorption. *Nat. Chem.* **5**, 300–306 (2013).
22. Sheng, W. et al. Correlating hydrogen oxidation and evolution activity on platinum at different pH with measured hydrogen binding energy. *Nat. Commun.* **6**, 5848 (2015).
23. Zheng, J., Nash, J., Xu, B. & Yan, Y. Perspective—towards establishing apparent hydrogen binding energy as the descriptor for hydrogen oxidation/evolution reactions. *J. Electrochem. Soc.* **165**, H27–H29 (2018).
24. Giles, S. A. et al. Recent advances in understanding the pH dependence of the hydrogen oxidation and evolution reactions. *J. Catal.* **367**, 328–331 (2018).
25. Ledezma-Yanez, I. et al. Interfacial water reorganization as a pH-dependent descriptor of the hydrogen evolution rate on platinum electrodes. *Nat. Energy* **2**, 17031 (2017).
26. Ryu, J. & Surendranath, Y. Tracking electrical fields at the Pt/H_2O interface during hydrogen catalysis. *J. Am. Chem. Soc.* **141**, 15524–15531 (2019).
27. Rebollar, L., Intikhab, S., Snyder, J. D. & Tang, M. H. Kinetic isotope effects quantify pH-sensitive water dynamics at the Pt electrode interface. *J. Phys. Chem. Lett.* **11**, 2308–2313 (2020).
28. Dekel, D. R. Unraveling mysteries of hydrogen electrooxidation in anion exchange membrane fuel cells. *Curr. Opin. Electrochem.* **12**, 182–188 (2018).
29. Tian, X., Zhao, P. & Sheng, W. Hydrogen evolution and oxidation: mechanistic studies and material advances. *Adv. Mater.* **31**, e1808066 (2019).
30. Lu, S. & Zhuang, Z. Investigating the influences of the adsorbed species on catalytic activity for hydrogen oxidation reaction in alkaline electrolyte. *J. Am. Chem. Soc.* **139**, 5156–5163 (2017).
31. McCrum, I. T. & Koper, M. T. M. The role of adsorbed hydroxide in hydrogen evolution reaction kinetics on modified platinum. *Nat. Energy* **5**, 891–899 (2020).
32. Feng, Z. et al. Role of hydroxyl species in hydrogen oxidation reaction: a DFT study. *J. Phys. Chem. C.* **123**, 23931–23939 (2019).
33. Dahal, A. & Batzill, M. Graphene–nickel interfaces: a review. *Nanoscale* **6**, 2548–2562 (2014).
34. Luo, M. et al. PdMo bimetallene for oxygen reduction catalysis. *Nature* **574**, 81–85 (2019).
35. Kambe, T. et al. Redox control and high conductivity of nickel bis(dithiolene) complex π-nanosheet: a potential organic two-dimensional topological insulator. *J. Am. Chem. Soc.* **136**, 14357–14360 (2014).
36. Dou, J. H. et al. Signature of metallic behavior in the metal–organic frameworks M_3(hexaiminobenzene)$_2$ (M = Ni, Cu). *J. Am. Chem. Soc.* **139**, 13608–13611 (2017).
37. Hammer, B. & Nørskov, J. K. Theoretical surface science and catalysis—calculations and concepts. *Adv. Catal.* **45**, 71–129 (2000).
38. Doyle, R. L., Godwin, I. J., Brandon, M. P. & Lyons, M. E. Redox and electrochemical water splitting catalytic properties of hydrated metal oxide modified electrodes. *Phys. Chem. Chem. Phys.* **15**, 13737–13783 (2013).
39. Qian, X. M. et al. A pulsed field ionization photoelectron–photoion coincidence study of the dissociative photoionization process $D_2O+h\nu \rightarrow OD^+ + D + e-$. *Chem. Phys. Lett.* **353**, 19–26 (2002).
40. Li, J. F. et al. Shell-isolated nanoparticle-enhanced Raman spectroscopy. *Nature* **464**, 392–395 (2010).
41. Deng, S. et al. Insight into the hydrogen oxidation electrocatalytic performance enhancement on Ni via oxophilic regulation of MoO_2. *J. Energy Chem.* **54**, 202–207 (2021).
42. Gao, L. et al. A nickel nanocatalyst within a h-BN shell for enhanced hydrogen oxidation reactions. *Chem. Sci.* **8**, 5728–5734 (2017).
43. Yang, F. et al. Enhanced HOR catalytic activity of PGM-free catalysts in alkaline media: the electronic effect induced by different heteroatom doped carbon supports. *J. Mater. Chem. A* **7**, 10936–10941 (2019).
44. Giles, S. A., Yan, Y. & Vlachos, D. G. Effect of substitutionally doped graphene on the activity of metal nanoparticle catalysts for the hydrogen oxidation reaction. *ACS Catal.* **9**, 1129–1139 (2018).
45. Yang, Y. et al. High-loading composition-tolerant Co–Mn spinel oxides with performance beyond 1 W/cm^2 in alkaline polymer electrolyte fuel cells. *ACS Energy Lett.* **4**, 1251–1257 (2019).
46. Wang, T. et al. Weakening hydrogen adsorption on nickel via interstitial nitrogen doping promotes bifunctional hydrogen electrocatalysis in alkaline solution. *Energy Environ. Sci.* **12**, 3522–3529 (2019).
47. Song, F. et al. Interfacing nickel nitride and nickel boosts both electrocatalytic hydrogen evolution and oxidation reactions. *Nat. Commun.* **9**, 4531 (2018).
48. Miller, H. A. et al. A Pd/C-CeO_2 anode catalyst for high-performance platinum-free anion exchange membrane fuel cells. *Angew. Chem. Int. Ed.* **55**, 6004–6007 (2016).

Methods

Materials. Nickel nitrate hexahydrate (99.9% Ni, ABCR), H_3BTC (>98%, TCI), cobalt(II) acetate tetrahydrate (>98%, Sigma-Aldrich), manganese(II) acetate tetrahydrate (≥99%, Sigma-Aldrich), hydrogen (99.999%, Carbagas) for the HOR test, ammonia (N38, Air Liquide) and ethanol (Tech grade, with 1% toluene, Thommen Furler) were used as received without further purification. *N*,*N*-Dimethylformamide (DMF, HPLC grade, Roth) was purified using a solvent purification system. H_2 for pyrolysis was generated with a H_2 generator equipped with a concentrated sulfuric acid trap to adsorb possible H_2O vapour. Supelco rotameters were purchased from Sigma-Aldrich.

Synthesis of nanocrystalline $Ni_3(BTC)_2$. $Ni_3(BTC)_2$ was prepared by a modification of a reported method[49]. H_3BTC (0.41 g, 2.0 mmol) and $Ni(NO_3)_2 \cdot 6H_2O$ (0.76 g, 2.6 mmol) were placed in different positions in a 45 ml Teflon-lined autoclave, and 30 ml anhydrous DMF was slowly added without any agitation. The autoclave was then sealed and kept at 120 °C for 12 h. The autoclave was opened after cooling to room temperature. The product mixture consisted of big bright-green crystals and a light-green powder. X-ray diffraction (XRD) analysis showed that only the light-green powder was the desired $Ni_3(BTC)_2$ (Supplementary Fig. 1). We were unable to identify the structure of the big crystals by single-crystal X-ray diffraction due to severe disorder. Because the powder was easily dispersed while the big crystals were not, they could be separated by first sonicating the solution and then discarding the supernatant (Supplementary Fig. 3). The final product was obtained by centrifuging the dispersion, washing three times with ethanol and then drying at 70 °C overnight. The yields of $Ni_3(BTC)_2$ and the side-product crystals were 40.6 and 13.9%, respectively, based on the metal. The product is very sensitive to water vapour, so it should be stored in a dry atmosphere. Note that the temperature used for the synthesis of $Ni_3(BTC)_2$ was 120 °C, which is below the boiling point of DMF. Thus, the synthesis can be scaled up by using air-tight glassware with a larger volume. The product selectivity is sensitive to the extent of mixing of the nickel salt and the ligand before the synthesis. A higher selectivity toward $Ni_3(BTC)_2$ was achieved when the two were separated. In contrast and in the extreme case, if both reactants were dissolved before heating, only the side product was obtained.

Synthesis of Ni-H_2-NH_3, Ni-H_2 and Ni-NH_3. The catalysts were prepared by temperature-programmed pyrolysis of $Ni_3(BTC)_2$ under a gas flow. Typically, for the synthesis of Ni-H_2-NH_3, 20 mg $Ni_3(BTC)_2$ was added to a crucible and placed in the centre of a pipe furnace. The furnace was first purged with N_2 for 10 min and then heated to 175 °C at a ramp rate of 10 °C min^{-1} under a mixed gas flow of 21.6 ml min^{-1} H_2 and 289.0 ml min^{-1} N_2. When the temperature reached 175 °C, 157.0 ml min^{-1} NH_3 was introduced into the reaction. The oven continued to be heated to 390 °C and was then kept at this temperature for 1 h before finally cooling to room temperature under a N_2 atmosphere. Before taking the product out of the furnace, a small amount of ethanol was injected into the crucible through a long syringe needle to prevent pyrophoric reoxidation of the catalyst (exception: to minimize surface oxidation and passivation, samples for the H_2 adsorption measurements were directly transferred to a glove box without being taken out of the tube furnace). After drying under a flow of N_2, the samples were collected and stored in an inert atmosphere.

The Ni-H_2 and Ni-NH_3 catalysts were prepared similarly to Ni-H_2-NH_3, but by using gas mixtures of H_2/N_2 (4.6:95.4, v/v) and NH_3/N_2 (33.6:66.4, v/v), respectively.

The gas flows were monitored using Supelco rotameters with needle valves. Glass, stainless steel and carboloy were used as float material for H_2, NH_3 and N_2, respectively. The flow rates were calculated on the basis of the scale readings of the rotameter with a flow data sheet (provided by the rotameter manufacturer). The exact scale readings for H_2, NH_3 and N_2 were 62, 105 and 111, respectively.

Preparation of C-H_2-NH_3, C-H_2 and C-NH_3. The Ni-H_2-NH_3, Ni-H_2 and Ni-NH_3 samples were dispersed in 2 M HCl and stirred overnight to remove the Ni nanoparticles. The samples were washed with a mixture of H_2O and ethanol (1:2) three times, and then dispersed in ethanol for further characterization. They were labelled as C-H_2-NH_3, C-H_2 and C-NH_3, correspondingly.

Preparation of CoMn spinel. CoMn spinel was synthesized by a modification of a reported method[45]. Typically, $Co(OAc)_2 \cdot 4H_2O$ (135.5 mg) was first dissolved in 4 ml H_2O, then 64 mg oxidized Vulkan XC-72R carbon dispersed in 30 ml ethanol was added. The mixture was sonicated for 10 min. Next, 0.44 ml ammonia and 24 ml ethanol were added dropwise. After sonicating the suspension for 10 min, a solution of 66.6 mg $Mn(OAc)_2 \cdot 4H_2O$ in 1.5 ml water was added. The final suspension was heated at 60 °C for 13 h under reflux and then transferred to a Teflon-lined autoclave for hydrothermal reaction at 150 °C for 3 h. The CoMn spinel/C product was collected by centrifugation, washed with ethanol and then dried under vacuum.

Materials characterization. TEM was carried out on a FEI Tecnai Osiris electron microscope equipped with a high-brightness field emission gun and an energy-dispersive X-ray spectroscopy analyser. The TEM samples were prepared by drop-drying the catalysts on ultrathin carbon-coated copper grids.

Powder XRD (PXRD) patterns of the catalysts were recorded on a PANalytical Aeris diffractometer using monochromatic Cu Kα radiation ($\lambda = 1.540598$ Å). The PXRD samples were prepared by drop-drying samples on amorphous silicon substrates.

XPS measurements were carried out using a PHI VersaProbe II scanning XPS microprobe.

UPS He II spectra were acquired at an excitation energy of 40.82 eV using a SPECS Leybold EA 11 MCD hemispherical electron analyser in ultrahigh vacuum conditions with a base pressure of 5×10^{-10} mbar. The binding energy scale was calibrated by measuring the Fermi level of an Au sample. The samples were subjected to soft Ar ion sputtering of 1 kV for a duration of 30 s to remove surface oxide and other contamination.

Thermogravimetric analysis (TGA) measurements were carried out on a Perkin Elmer TGA 4000 instrument. Samples were heated from 30 to 900 °C at a ramp rate of 5 °C min^{-1}, and the temperature was then maintained at 900 °C for 5 min under an air flow of 20 ml min^{-1}. After the analysis, the residue was collected for PXRD analysis to determine the phase.

Raman spectra were recorded on a RENISHAW inVia confocal Raman microscope. The scattered light was collected with a charge-coupled device detector. Prior to each use, the Raman shift was calibrated by measuring Si as the internal standard. SHINER spectroscopy was applied for in situ measurement[40]. An extra electrochemical cell was mounted on the sample stage, and 0.01 M KOH or KOD was used as the electrolyte with H_2 purging. Before recording the signal, the sample was reduced at −0.3 V versus RHE for 3 min to remove the surface oxide layer.

Conductivity was measured in ambient air by the four-point probe method using a Keithley 2400 source measuring unit with a four-wire set-up. Ni/C circular pellets with a diameter of 13 mm were prepared under a pressure of 590 Mpa (8 ton-force) for the conductivity measurements.

H_2 adsorption isotherms were measured at 35 °C between 2 and 600 mbar on a Micromeritics 3 Flex instrument. The sample (300 mg) was loaded in a glass cell inside a nitrogen-filled glove box, transferred to the instrument and dried in situ under vacuum (<10^{-3} mbar) at 120 °C for 1 h. After cooling to 35 °C under vacuum, a leak test was performed prior to analysis. The quantities adsorbed (Q_i, unit: $cm^3\ g^{-1}$) and adsorption constants (k_i; unit: mm Hg^{-1}) were extracted by fitting a dual Langmuir adsorption model (Matlab) to account for weak ($k < 0.01$) and strong adsorption ($k > 1$).

Electrochemical measurements. All electrochemical measurements were performed in a standard three-electrode system controlled by either a CHI 760E or Gamry electrochemical workstation. All the data were *iR*-corrected. A KCl-saturated Ag/AgCl electrode was used as the reference electrode, and a clean platinum wire was used as the counter electrode. During the HER stability test, an extra frit was used for the counter electrode to prevent Pt contamination. HOR measurements were performed in H_2-saturated 0.1 M KOH, and the catalyst ink was cast onto a 5-mm-diameter glassy carbon RDE to form a thin film layer (0.28 mg catalyst per cm^2 (0.28 $mg_{cat}\ cm^{-2}$)). HER measurements were performed in 1 M KOH using 3-mm-diameter glassy carbon as the working electrode with a loading of 0.42 $mg_{cat}\ cm^{-2}$. Electrochemical impedance spectroscopy measurements were carried out using a.c. voltage with a 5 mV amplitude in 1 M KOH solution at $\eta = 100$ mV. The frequency range was from 0.1 MHz to 0.1 Hz. For the HER and HOR measurements, the scan rate was 1 mV s^{-1}, whereas for the CV measurements, the scan rate was 50 mV s^{-1}. Unless specified, all the potentials given in this paper are referenced to the RHE potential, which was calibrated by LSV scans with Pt/C as the working electrode in H_2-saturated electrolyte. Before any electrochemical measurement, the electrode was activated by performing CV scans from −0.02 to 0.05 V versus RHE for five cycles to remove surface oxygen species on nickel.

To calculate the kinetic current density, the Koutecky–Levich equation (equation (1)) was used to describe a process controlled by both kinetics and diffusion ($j < 0.8 j_d$):

$$\frac{1}{j} = \frac{1}{j_k} + \frac{1}{j_d} = \frac{1}{j_k} + \frac{1}{Bc_0\omega^{1/2}} \quad (1)$$

where j_k is the kinetic current density and j_d is the diffusion-limited current density, B is the Levich constant, c_0 is the solubility of H_2 in the electrolyte, and ω is the rotating speed. j_d can be further expanded according to the Levich equation (equation (2)):

$$j_d = 0.62nFD^{2/3}\nu^{-1/6}c_0\omega^{1/2} = Bc_0\omega^{1/2} \quad (2)$$

where n is the electron transfer number during the reaction, F is Faraday's constant, D is the diffusion coefficient of H_2 and υ is the kinematic viscosity of 0.1 M KOH. These four factors as well as the constant 0.62 in equation (2) can be simplified by replacing with the Levich constant B. By fitting the current density at an overpotential of 25 mV to equation (1), we obtained the value of $(Bc_0)^{-1}$ as 4.86 $cm^2\ mA^{-1}\ s^{-1/2}$ (Supplementary Fig. 11), close to the theoretical value of 4.87 $cm^2\ mA^{-1}\ s^{-1/2}$ (ref. [50]). Using this value of $(Bc_0)^{-1}$, we can calculate j_k at other potentials within the range where equation (1) is applicable. For the HOR measured in 1 M KOH, $(Bc_0)^{-1}$ was obtained using the limiting current density by applying equation (2), and was calculated to be 6.83 $cm^2\ mA^{-1}\ s^{-1/2}$.

The exchange current density j_0 can be obtained by fitting j_k and η to the Butler–Volmer equation (equation (3)):

$$j_k = j_0 \left(e^{\frac{\alpha F}{RT}\eta} - e^{\frac{(\alpha-1)F}{RT}\eta} \right) \quad (3)$$

where α is charge transfer coefficient, F is Faraday's constant (96,485 C mol^{-1}), R is the universal gas constant (8.314 J mol^{-1} K^{-1}), T is the temperature and η is the overpotential. The obtained Tafel plot is shown in Fig. 2b. Extrapolating the curve with fitted j_0 and α, we can calculate j_k at potentials where equation (1) can no longer be applied. Here, j_k was calculated for Ni-H_2-NH_3 at $\eta = 50$ mV using this method.

Membrane electrode assembly measurement. The electrode ink was prepared by adding the catalyst, additional Vulcan XC-72 carbon for anode ink only and ionomer to isopropanol as solvent, followed by sonication for 1 h. The weight ratio of the Vulcan XC-72 carbon and Ni-H_2-NH_3 catalyst was 1:1, and the weight ratio of the PAP-TP-100 (*N*-methyl-4-piperidium group and terphenyl group in a molar ratio of 1.0) ionomer and carbon support was 0.33 for both the anode and cathode. Next, the ink including Ni was sprayed onto Sigracet SGL 25BA carbon paper by airbrush to produce a gas diffusion electrode of 5 cm^2 for the anode, while the ink including spinel catalyst was sprayed onto the PAP-TP-85 (*N*-methyl-4-piperidone and terphenyl monomers in a molar ratio of 0.85) membrane (18 ± 2 μm) to produce a catalyst-coated membrane of 5 cm^2 for the cathode. The final catalyst loading was 6.4 mg_{Ni} cm^{-2} for the anode and 1.2 mg_{cat} cm^{-2} for the CoMn spinel catalyst. After drying at room temperature, the MEA was immersed in 2 M KOH aqueous solution for 0.5 h to remove CO_2 absorbed by the catalyst layers. The residual KOH solution on the MEA would then be rinsed before testing.

The MEA was assembled with a fluorinated ethylene propylene gasket, a piece of carbon paper (Sigracet SGL 29 BC) as the gas diffusion layer on the cathode side, a graphite bipolar plate with 5 cm^2 flow field (ElectroChem) and a gold-coated current collector on each side to complete the full HEMFC. A fuel cell test station (Scribner 850e) with back-pressure regulators was used to measure the polarization curves and stability under H_2/O_2 or H_2/CO_2-free air conditions.

Data availability

All data are available in the main text and the Supplementary Information, and source data are deposited in Zenodo repository (https://doi.org/10.5281/zenodo.5885289)[51]. Source data are provided with this paper.

References

49. Wade, C. R. & Dinca, M. Investigation of the synthesis, activation, and isosteric heats of CO_2 adsorption of the isostructural series of metal–organic frameworks $M_3(BTC)_2$ (M = Cr, Fe, Ni, Cu, Mo, Ru). *Dalton Trans.* **41**, 7931–7938 (2012).
50. Sheng, W. C., Gasteiger, H. A. & Shao-Horn, Y. Hydrogen oxidation and evolution reaction kinetics on platinum: acid vs alkaline electrolytes. *J. Electrochem. Soc.* **157**, B1529–B1536 (2010).
51. Ni, W. et al. An efficient nickel hydrogen oxidation catalyst for hydroxide exchange membrane fuel cells. Source data at https://doi.org/10.5281/zenodo.5885289 (2022).

Acknowledgements

W.N. and X.H. acknowledge the financial support of EPFL; T.W. and Y.Y. acknowledge the financial support of the US Department of Energy, Advanced Research Projects Agency-Energy (award nos. DE-AR0000771, DE-AR0000805, DE-AR0001034 and DE-AR0001149); F.H. and J.S.L. acknowledge the financial support of the European Research Council under the European Union's Horizon 2020 research and innovation program (starting grant CATACOAT, no. 758653) as well as the Swiss National Science Foundation (grant no. PYAPP2_15428); S.L. acknowledges the Marie Skłodowska-Curie Fellowship (grant no. 838367). We thank P. A. Schouwink (EPFL) for assistance with XRD measurements.

Author contributions

W.N. designed and synthesized all the catalysts, performed electrochemical measurements and characterizations; T.W. assembled the MEAs and performed the fuel cell measurements; F.H. performed the chemisorption experiments and analysed the data with J.S.L.; A.K. performed the UPS measurements and analysed the data with A.S.; S.L. and W.N. performed the in situ Raman experiments; L.Y. performed the four-probe conductivity measurements; W.N. and X.H. wrote the paper, with input from all the other co-authors. Y.Y. and X.H. directed the research.

Competing interests

The authors declare no competing interests.

Additional information

Supplementary information The online version contains supplementary material available at https://doi.org/10.1038/s41563-022-01221-5.

Correspondence and requests for materials should be addressed to Yushan Yan or Xile Hu.

Peer review information *Nature Materials* thanks Frédéric Jaouen and Sanjeev Mukerjee for their contribution to the peer review of this work.